

# *P*–*V*–*T* equation of state of synthetic mirabilite ( $\text{Na}_2\text{SO}_4 \cdot 10\text{D}_2\text{O}$ ) determined by powder neutron diffraction

A. D. Fortes,<sup>a,b\*</sup> H. E. A. Brand,<sup>c</sup> L. Vočadlo,<sup>a,b</sup> A. Lindsay-Scott,<sup>a,b</sup> F. Fernandez-Alonso<sup>d,e</sup> and I. G. Wood<sup>a,b</sup>

<sup>a</sup>Centre for Planetary Sciences at UCL/Birkbeck, Gower Street, London WC1E 6BT, UK,

<sup>b</sup>Department of Earth Sciences, University College London, Gower Street, London WC1E 6BT, UK,

<sup>c</sup>Australian Synchrotron, 800 Blackburn Road, Clayton, VIC 3168, Australia, <sup>d</sup>ISIS Facility, STFC Rutherford Appleton Laboratory, Harwell Science and Innovation Campus, Chilton, Didcot,

Oxfordshire OX11 0QX, UK, and <sup>e</sup>Department of Physics and Astronomy, University College

London, Gower Street, London WC1E 6BT, UK. Correspondence e-mail: andrew.fortes@ucl.ac.uk

Neutron powder diffraction data have been collected from  $\text{Na}_2\text{SO}_4 \cdot 10\text{D}_2\text{O}$  (the deuterated analogue of mirabilite), a highly hydrated sulfate salt that is thought to be a candidate rock-forming mineral in some icy satellites of the outer solar system. These measurements, made using the OSIRIS instrument on the ISIS neutron spallation source, covered the range  $0.1 < P < 545$  MPa and  $150 < T < 270$  K. The refined unit-cell volumes as a function of pressure and temperature are parameterized in the form of a Birch–Murnaghan third-order equation of state, and the anisotropic linear incompressibilities are represented in terms of the elastic strain tensor. At 270 K, the bulk modulus  $K_{0,270} = 19.6$  (1) GPa, its first pressure derivative  $\partial K/\partial P = 5.8$  (5) and its temperature dependence  $\partial K/\partial T = -0.0175$  (6) GPa K<sup>-1</sup>. The stiffest direction at 270 K, with a linear bulk modulus of  $\sim 82$  GPa, is coincident with the twofold axis of this monoclinic crystal. Of the remaining two principal directions, the most compressible ( $K \simeq 44$  GPa) is roughly aligned with the *c* axis, and the intermediate value ( $K \simeq 59$  GPa) is therefore approximately collinear with **a**\*. With the aid of additional published data, a number of other important thermodynamic quantities have been derived, including the Grüneisen and Anderson–Grüneisen parameters, and the volume and enthalpy of melting along the high-pressure melting curve. Additional data obtained during this work, concerning the elastic properties of deuterated ice IV, are also presented.

© 2013 International Union of Crystallography  
Printed in Singapore – all rights reserved

## 1. Introduction

### 1.1. Background

Sodium sulfate decahydrate ( $\text{Na}_2\text{SO}_4 \cdot 10\text{H}_2\text{O}$ ) is the stable phase in contact with an equilibrium mixture of  $\text{Na}_2\text{SO}_4$  and  $\text{H}_2\text{O}$  at room pressure between a eutectic with ice Ih at 272.868 K and a melting point at 305.533 K (Richards & Wells, 1902; Hartley *et al.*, 1908), occurring naturally as the mineral mirabilite. Salt hydrates such as the title compound typically occur in a range of stable and metastable hydration states as a function of both pressure and temperature (*e.g.* Sood & Stager, 1966); this degree of compositional freedom allows for systematic studies aimed at isolating the contributions of ionic bonding and hydrogen bonding to the physical properties of the material. In the  $\text{Na}_2\text{SO}_4$ – $\text{H}_2\text{O}$  system, a metastable heptahydrate ( $\text{Na}_2\text{SO}_4 \cdot 7\text{H}_2\text{O}$ ) has been known for over a century but was characterized in detail only very recently (Oswald *et al.*, 2008; Hamilton & Hall, 2008; Hall & Hamilton, 2008; Hamilton & Menzies, 2010; Derluyn *et al.*, 2011; Saidov

*et al.*, 2012), and an octahydrate ( $\text{Na}_2\text{SO}_4 \cdot 8\text{H}_2\text{O}$ ) was reported by Oswald *et al.* (2008) as the stable phase formed at 1.54 GPa. Although the  $\text{Na}_2\text{SeO}_4$ – $\text{H}_2\text{O}$  system is qualitatively identical to the  $\text{Na}_2\text{SO}_4$ – $\text{H}_2\text{O}$  system (Funk, 1900; Meyer & Aulich, 1928), there are other stable hydration states in the  $\text{Na}_2\text{CrO}_4$ ,  $\text{Na}_2\text{MoO}_4$  and  $\text{Na}_2\text{WO}_4$ – $\text{H}_2\text{O}$  systems;  $\text{Na}_2\text{CrO}_4 \cdot 10\text{H}_2\text{O}$  melts incongruently to a hexahydrate at 292.675 K and then to a tetrahydrate at 299.05 K (Richards & Kelley, 1911), whilst both  $\text{Na}_2\text{MoO}_4 \cdot 10\text{H}_2\text{O}$  and  $\text{Na}_2\text{WO}_4 \cdot 10\text{H}_2\text{O}$  melt incongruently to a dihydrate, at 283.43 and 279 K, respectively (Funk, 1900; Cadbury, 1955; Zhilova *et al.*, 2008). Extensive substitution of sulfate into these alternative hydrates has been reported (Richards & Meldrum, 1921; Cadbury *et al.*, 1941; Cadbury, 1945).

Mirabilite undergoes a well characterized dehydration reaction (incongruent melting) to one of the numerous polymorphs of anhydrous sodium sulfate (Rasmussen *et al.*, 1996; Bobade *et al.*, 2009), the *Fddd* phase known as  $\text{Na}_2\text{SO}_4$ -V, which is the mineral thenardite. This transition was the initial

target of high-pressure studies; investigations up to  $\sim 300$  MPa (Tammann, 1903*a,b*; Block, 1913) revealed a broad maximum in the melting temperature,  $T_m$ , at approximately 100 MPa, above which  $T_m$  falls, a pressure dependence that denotes a switch in sign of the volume change on melting,  $\Delta V_m$ . Subsequently, this high-pressure melting curve with negative  $\partial T/\partial P$  was extended up to  $\sim 800$  MPa (Geller, 1924; Tammann, 1929; Gibson, 1942; Kryukov & Manikhin, 1960). More recently, attention has shifted to the pressure dependence of the ice–mirabilite eutectic, which roughly follows the pressure melting curve of pure water ice (Hogenboom *et al.*, 1999; Dougherty *et al.*, 2006, 2011, 2012). Over the range between the eutectic and the melting point, the shift in solubility with pressure was predicted over 70 years ago (Adams, 1938), using a prescient educated guess for the compressibility of mirabilite ( $4 \times 10^{-6} \text{ bar}^{-1}$ ; 1 bar =  $10^5$  Pa), and was measured up to 500 MPa by Tanaka *et al.* (1992). Kryukov & Manikhin (1960) confirmed the prediction of Adams (1938) that mirabilite switches from incongruent to congruent melting above 500 MPa.

The phase behaviour of the  $\text{Na}_2\text{SO}_4\text{--H}_2\text{O}$  system is evidently complex, and this complexity is likely to have important consequences for the structure and dynamics of large icy planetary bodies, where sodium sulfate hydrates are expected to be ‘rock-forming’ minerals (*e.g.* Kargel, 1991; Fortes & Choukroun, 2010; see *Discussion* below). However, there remains a substantial gap in our knowledge of mirabilite’s properties, which must be closed in order to address significant problems in planetary modelling, specifically the equation of state. The situation remarked upon by Adams (1938), that ‘... the compression ... of  $\text{Na}_2\text{SO}_4 \cdot 10\text{H}_2\text{O}$  has not yet been determined’, has remained true until now, and yet the density of the solid hydrate along the melting curve and along the high-pressure eutectics is fundamental to computing the buoyancy of ‘igneous’ melts and the partial freezing behaviour of global subsurface oceans in the interiors of icy planetary bodies. Furthermore, the density of the solid is required in order to calculate accurately the radial density structure of a model icy satellite.

We have been engaged in a programme to study the high-pressure behaviour of candidate ‘planetary’ ices and hydrates, as part of which we have measured the thermal expansion of mirabilite from 4 to 300 K (Brand *et al.*, 2009), carried out a single-crystal structural study as a function of temperature at room pressure (Wood *et al.*, 2010) and used density functional theory (DFT) calculations to simulate the material at high pressures (Brand *et al.*, 2010). The computational study yielded the first quantification of the bulk elastic properties and of the highly anisotropic compressional behaviour.

## 1.2. Experimental objectives

The objective of this work was to determine the unit-cell parameters of mirabilite as a function of both pressure and temperature in order to fit a thermal equation of state (EOS). This EOS should yield accurate densities for calculation of important thermodynamic quantities such as volume and

enthalpy changes along the high-pressure transition lines (see our similar study of ice VI; Fortes *et al.*, 2012) and thermoelastic quantities such as the Grüneisen and Anderson–Grüneisen parameters [see, for example, our study of (Mg,Fe)O; Wood *et al.*, 2008]. The most efficient technique to carry out this work over the relatively low pressure range of interest (0.1–550 MPa) is to use the neutron powder diffraction method upon a sample contained in a gas-pressure vessel. A necessary consequence of using neutron diffraction to obtain high-resolution data from a specimen in a complex  $P$ ,  $T$  sample environment is the requirement to use a deuterated analogue,  $\text{Na}_2\text{SO}_4 \cdot 10\text{D}_2\text{O}$ , in order to eliminate the undesirable incoherent neutron scattering from  $^1\text{H}$ . Although it is known that there is a small difference between protonated *versus* deuterated mirabilite in the transition temperature – the decadeuterate melts incongruently at 307.63 K (Taylor, 1934) – the question of whether there is any significant difference in the molar volume is deferred to the *Discussion* (§4).

As a result of prior experience, we chose to carry out this work using the OSIRIS instrument (Telling & Andersen, 2005, 2008) at the ISIS neutron spallation source, Rutherford Appleton Laboratory, UK. Although nominally an inelastic spectrometer, OSIRIS is equipped with a bank of back-scattering detectors for high-resolution powder diffraction experiments. OSIRIS views a 20 K liquid-hydrogen moderator and thus receives a very high flux of colder (longer-wavelength) neutrons, making it well suited to the study of low-symmetry materials with large unit cells. In order to achieve such long- $d$ -spacing observations without frame overlap, the instrument has a series of user-controlled chopper phasings which select different flight-time windows, each with the same bandwidth but with a different central wavelength. For example,  $d$  range 2 covers the neutron time-of-flight window from 29.4 to 69.4 ms, yielding a powder pattern with  $d$  spacings from 1.8 to 4.0 Å in the backscattering detectors ( $150 < 2\theta < 171^\circ$ , resolution  $\Delta d/d = 6 \times 10^{-3}$ );  $d$  range 3 covers 47.1–87.1 ms (2.9–4.9 Å), and so on. The preparation of our samples and commission of the experiment are described in the following section.

## 2. Experimental method

Crystals of  $\text{Na}_2\text{SO}_4 \cdot 10\text{D}_2\text{O}$  were prepared from a supersaturated solution of  $\text{Na}_2\text{SO}_4$  (Sigma S9627, ReagentPlus,  $\geq 99.0\%$ ) in heavy water (Aldrich 435767, 99 at.% D). An initial deposit of very fine grained crystals was coarsened by temperature cycling (in the range 283–298 K) over a period of a few weeks. These larger crystal grains were then extracted from the mother liquid and quickly dried on filter paper in air at room temperature. The dried crystals were immediately immersed in liquid nitrogen in a steel cryomortar and ground to a powder with a nitrogen-cooled steel pestle. In our previous studies of this material, we found that grinding under air, even in a refrigerated room, tended to produce a damp paste – which was more likely to develop a preferred orientation when pressed into a sample can – rather than a dry

powder; grinding under liquid nitrogen produces a much better powder. This powder was spooned into a TiZr null-scattering-alloy pressure vessel embedded in dry-ice snow. The pressure vessel was kept at dry-ice temperatures whilst it was screwed onto a cryostat centre stick and fitted with copper collars (top and bottom), RhFe resistance thermometers and heaters to allow temperature control. This assembly was then inserted into a standard orange cryostat of 100 mm bore, mounted on the OSIRIS beamline and equilibrated at 270 K under 23 MPa of He gas.

First inspection of the powder diffraction data revealed that the specimen consisted primarily of mirabilite with a small admixture of ice Ih (later determined to be ~5 wt%). Proceeding from this point, the experiment was conducted in four distinct stages, as outlined below, with data being collected in *d* range 2 and *d* range 3 (see above), each for approximately 1 h 45 min (equivalent to 130  $\mu$ A of integrated proton current at the instrument's 25 Hz operating frequency in each time window).

(1) Data were first acquired as the He-gas pressure was increased from 23 to 80, 140 and 200 MPa, with subsequent measurements in 50 MPa increments up to the maximum operating pressure of the gas cell, 550 MPa. We observed that the coexisting ice Ih melted when the pressure was increased from 20 to 80 MPa, as expected from the negative slope of the melting curve,  $\partial T_m/\partial P$  (e.g. Dougherty *et al.*, 2012). Approximately half-way through the measurement at 253 MPa, the ISIS synchrotron suffered a mains power failure, which resulted in loss of beam for 64 h. Furthermore, the power cut caused the He intensifier to lose pressure, resulting in complete decompression of the specimen. Once power was restored, the intensifier was reset and the pressure brought back to ~250 MPa; the experiment resumed with continued compression up to 550 MPa.

(2) The sample was then cooled down the 550 MPa isobar to 150 K, with data being collected in 20 K increments. Upon cooling from 270 to 250 K, additional Bragg peaks appeared in the diffraction pattern, which we identified as the metastable ice polymorph ice IV (Engelhardt & Whalley, 1972).

(3) Upon reaching 150 K, the gas pressure was reduced in 100 MPa increments to 80 MPa, and finally decreased to atmospheric pressure (100 kPa). Ice IV underwent decompression-induced melting below 100 MPa (*cf.* Mishima & Stanley, 1998). However, this supercooled liquid crystallized when the pressure was reduced to 100 kPa, forming stacking-disordered ice Ic. The latter was identified by the occurrence of a broad amorphous feature in the background centred around the expected position of the 111 reflection of the cubic ice phase (Hansen *et al.*, 2008; Malkin *et al.*, 2012).

(4) A final series of measurements were made at 100 kPa on warming to 210 K and finally to 270 K. The last datum was measured in *d* ranges 2 and 3 for 220  $\mu$ A (approximately 3 h) in each time window. The stacking-disordered ice Ic phase transformed to ideal ice Ih during warming from 150 to 210 K.

The powder diffraction data were normalized to the incident monitor, corrected for instrumental efficiency using data from a vanadium standard, and finally corrected for the

substantial wavelength-dependent absorption of the TiZr vessel by subtraction of a histogram collected from the empty pressure cell at 270 K. We discovered that application of the 270 K empty-cell subtraction to data measured below 270 K resulted in some data points having negative values. An arbitrary constant was therefore added to these diffraction patterns to ensure that all useful parts of the pattern had positive values. These data were exported in a format suitable for analysis with the *GSAS/EXPGUI* software package (Larsen & Von Dreele, 2000; Toby, 2001). The diffraction data were fitted initially using the Rietveld method (to obtain accurate peak shifts from one *P* or *T* increment to the next) and the least-squares minimization was then run to convergence using the structure-independent '*F*<sub>calc</sub>-weighted' profile-refinement method, varying only the peak-profile coefficients and unit-cell parameters of the phases present (mirabilite and ice Ih, ice Ic or ice IV). The first complete round of refinements yielded unit-cell volumes for mirabilite ~0.75% larger (at a given temperature) than we had found previously in our high-resolution powder study of mirabilite as a function of temperature at ambient pressure (Brand *et al.*, 2009). This difference, equivalent to the volume change effected by application of -150 MPa, was eliminated by fixing the unit-cell parameters in the final 100 kPa, 270 K data set at our published value for this *P*, *T* point (Brand *et al.*, 2009) and refining the diffractometer constants DIFC and DIFA (Fig. 1). All of the refinements were re-run with the newly determined neutron flight path to yield the values used in our following analysis. The matter of the absolute accuracy of the unit-cell volumes obtained from these two powder instruments will be returned to in the *Discussion* (§4).

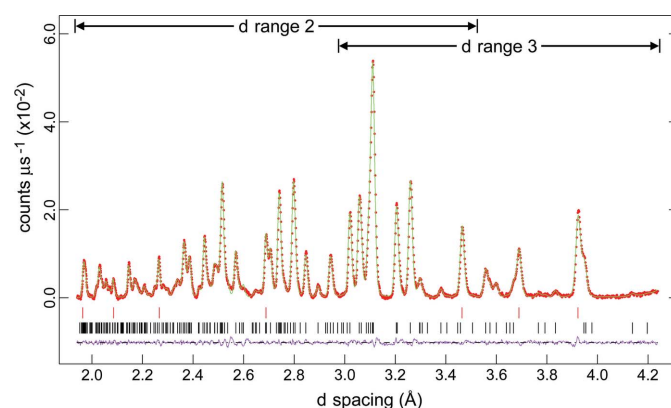


**Figure 1** Background-subtracted neutron powder diffraction pattern collected from a mixture of 95 wt% deuterated mirabilite and 5 wt% ice Ih at 0.1 MPa and 270 K (shown in colour in the electronic version of the journal). Filled circles (red in the electronic version) show the measurements, the line through the data (green) is the fitted profile and the line at the bottom (purple) is the difference curve. Tick marks indicate the positions of Bragg peaks due to ice Ih (top, in red) and mirabilite (bottom, in black). This figure combines data from two 40 ms-wide time-of-flight windows (*d* range 2 and *d* range 3; see text). Compare these diffraction data, both in terms of resolution and intensities, with Fig. 2 of Brand *et al.* (2009).

**Table 1**

Parameters obtained by fitting equations (1)–(5) either to the OSIRIS data alone or to the combined OSIRIS and HRPD data sets.

Values in parentheses are errors on the least significant digits.

	MILEOS $P$ – $V$ – $T$ fit (OSIRIS data only)	MILEOS $P$ – $V$ – $T$ fit (OSIRIS + HRPD data)	BMEOS3 $P$ – $V$ – $T$ fit (OSIRIS + HRPD data)
$V_{0,270}$ (Å <sup>3</sup> )	1455.65 (12)	1455.795 (29)	1455.793 (35)
$x_1$ (Å <sup>3</sup> K <sup>−1</sup> )	$1.334 (46) \times 10^{-1}$	$1.3857 (9) \times 10^{-1}$	$1.3842 (10) \times 10^{-1}$
$x_2$ (Å <sup>3</sup> K <sup>−2</sup> )	$2.03 (36) \times 10^{-4}$	$2.173 (60) \times 10^{-4}$	$2.164 (66) \times 10^{-4}$
$K_{0,270}$ (GPa)	19.67 (27)	19.58 (12)	19.59 (13)
$\partial K/\partial T$ (GPa K <sup>−1</sup> )	−0.0147 (13)	−0.0176 (6)	−0.0175 (6)
$K'_{0,270}$	5.84 (100)	5.75 (48)	5.79 (53)

**Table 2**

Parameters obtained by fitting equations (2)–(5) either to the OSIRIS data alone or to the combined OSIRIS and HRPD data sets (see table footnote and main text for details) for each of the three crystallographic axes, the orthogonal direction  $a \sin \beta$  and the unit-cell volume.

The lowermost rows report the *ab initio* values of the bulk modulus and its first pressure derivative (Brand *et al.*, 2010).

	$a$ axis†	$b$ axis‡	$c$ axis§	$a \sin \beta$ ¶	Unit-cell volume¶
Experimental $P$ – $V$ – $T$					
$X_{0,270}$ (Å or Å <sup>3</sup> )	11.5011 (2)	10.3621 (3)	12.8266 (3)	10.9535 (1)	1455.79 (4)
$x_1$ (Å or Å <sup>3</sup> K <sup>−1</sup> )	$4.15 (7) \times 10^{-4}$	$1.03 (5) \times 10^{-4}$	$6.16 (9) \times 10^{-4}$	$3.89 (4) \times 10^{-4}$	$1.38 (1) \times 10^{-1}$
$x_2$ (Å or Å <sup>3</sup> K <sup>−2</sup> )	$1.3 (1) \times 10^{-6}$	0	$1.26 (6) \times 10^{-6}$	$4.9 (2) \times 10^{-7}$	$2.16 (7) \times 10^{-4}$
$x_3$ (Å or Å <sup>3</sup> K <sup>−3</sup> )	$3.5 (6) \times 10^{-9}$	0	0	0	0
$K_{0,270}$ (GPa)	54.0 (6)	81.7 (6)	44.6 (6)	57.7 (5)	19.6 (1)
$\partial K/\partial T$ (GPa K <sup>−1</sup> )	−0.057 (3)	−0.08 (3)	−0.026 (3)	−0.086 (3)	−0.0175 (6)
$K'_{0,270}$	15 (2)	21 (fixed)	25 (3)	16 (2)	5.8 (5)
$\partial K'/\partial T$ (K <sup>−1</sup> )	0	0.23 (9)	0	0	0
$R^2$	0.99976	0.99957	0.99975	0.99980	0.99991
DFT (athermal)					
$K_{0,0}$ (GPa)	70 (1)	92 (4)	55 (2)	76 (1)	22.2 (1)
$K'_{0,0}$	16.3 (3)	21 (2)	10 (1)	17.9 (5)	5.6 (1)

† Fitted to all OSIRIS data and HRPD warming and cooling data in the range 100–300 K (65 data points). ‡ Fitted only to the OSIRIS data (25 data points). § Fitted to OSIRIS data (excluding 23 and 80 MPa at 270 K) and HRPD warming data in the range 100–300 K (44 data points). ¶ Fitted to OSIRIS data (excluding 23 and 80 MPa at 270 K) and HRPD warming and cooling data in the range 100–300 K (63 data points).

### 3. Results

#### 3.1. Mirabilite $P$ – $V$ – $T$ equation of state

Using the powder diffraction data collected on OSIRIS, the unit-cell parameters of deuterated mirabilite were refined to a precision of between 1 and 3 parts in 100 000 at 25 state points (Supplementary Table S1<sup>1</sup>). In addition to these data, we have included in our analysis another 21 points collected on warming from 100 to 300 K at room pressure and 19 points collected on cooling from 295 to 105 K at room pressure; these measurements, with approximately two–three times greater precision, were made by us previously with the High Resolution Powder Diffractometer (HRPD) at ISIS and reported by Brand *et al.* (2009). An observation that is worth restating from the earlier work is the difference in behaviour of the crystal between measurements made upon slow warming of

<sup>1</sup> Supplementary tables and figures are available from the IUCr electronic archives (Reference: HE5569). Services for accessing this material are described at the back of the journal.

the specimen after it had been rapidly cooled to 4 K and measurements made afterwards during slow cooling from room temperature. These differences are substantial in the case of the  $b$  axis and the monoclinic angle  $\beta$  below 150 K, and small but nonetheless significant for the  $c$  axis. These differences were attributed by us to freezing in of the dynamically disordered sulfate oxyanion's orientation and the associated hydrogen bonds accepted by this polyhedral unit from the surrounding water molecules (Ruben *et al.*, 1961; Levy & Lisensky, 1978). We therefore were aware of the possibility that unit-cell parameters refined to match the HRPD data at 270 K might not necessarily 'marry up' with the HRPD data at 150 K after compression, cooling and decompression. Indeed, for both the  $b$  and the  $c$  axis this was the case: the OSIRIS  $b$ -axis value at 150 K did not agree with either the warming or the cooling value obtained on HRPD; the OSIRIS  $c$ -axis length did agree with the HRPD warming value. Hence we were forced to be selective in our combination of the two data sets for fitting of a  $P$ – $V$ – $T$  EOS (see Table 1 and footnote in Table 2).

As we did previously in our study of the  $P$ – $V$ – $T$  equation of state of ice VI (Fortes *et al.*, 2012) we began with a straightforward parameterization based upon the Murnaghan integrated linear equation of state (MILEOS; Murnaghan, 1944):

$$V_{P,T} = V_{0,T} / [P(K'_{0,T}/K_{0,T}) + 1]^{1/K'_{0,T}}, \quad (1)$$

where

$$V_{0,T} = V_{0,270} + x_1 T^* + x_2 T^{*2} + x_3 T^{*3}, \quad (2)$$

$$K_{0,T} = K_{0,270} + (\partial K/\partial T)_P T^*, \quad (3)$$

$$K'_{0,T} = K'_{0,270} + (\partial K'/\partial T)_P T^*. \quad (4)$$

In the equations above, the reference temperature  $T^* = T - 270$  K, the quantity  $K$  is the isothermal bulk modulus, and  $K'$  is the first pressure derivative of the bulk modulus,  $(\partial K/\partial P)_T$ . The reference temperature of 270 K was chosen so as to minimize the propagated errors along the various melting lines discussed in §4, which lie roughly within  $\pm 30$  K of 270 K. The MILEOS has the advantage over Birch–Murnaghan formulations in that the dependent variable may easily be chosen as  $V$  rather than  $P$ , allowing for computation of the propagated error in  $V$  at a given  $P$ ,  $T$  point, which is the

desirable situation in most practical applications of these equations of state.

Equation (4) provides for the possibility that  $K'$  exhibits some temperature dependence; this was found to be true only for the  $b$  axis. Whilst the  $b$  axis of mirabilite stiffens with pressure at 270 K (*i.e.*  $K'$  is positive), this direction softens with pressure at 150 K (*i.e.*  $K'$  becomes negative; see Supplementary Figs. S1 and S3). This peculiar situation means that, at some intermediate temperature, equation (1) cannot be evaluated, since the function has a singularity at  $K' = 0$ ; we are therefore forced instead to adopt the Birch–Murnaghan equation of state (BMEOS) where such singularities do not occur. For completeness, therefore, we have used the third-order BMEOS [BMEOS3; equation (5)] (Birch, 1952) to fit the unit-cell volume and each of the three crystallographic axes (as well as the direction  $a^* = a \sin \beta$ ), and we report here both the MILEOS and the BMEOS3  $P$ – $V$ – $T$  fits for the unit-cell volume (Table 1). With the exception of the thermal expansion term  $x_1$  [equation (2)], these two functions yield parameters within  $1\sigma$  of each other. Furthermore, the calculated unit-cell volumes along the pressure–melting curve (see §4) differ by just one-tenth of the propagated error on the MILEOS-computed volumes; for all practical purposes, therefore, these two parameterizations may be considered identical:

$$P = \left(\frac{3}{2}\right) K_{0,T} \left[ \left(\frac{V_{0,T}}{V_{P,T}}\right)^{7/3} - \left(\frac{V_{0,T}}{V_{P,T}}\right)^{5/3} \right] \times \left\{ 1 + \frac{3}{4} (K'_{0,T} - 4) \left[ \left(\frac{V_{0,T}}{V_{P,T}}\right)^{2/3} - 1 \right] \right\}. \quad (5)$$

The two thermal EoSs [equations (2)–(5)] were fitted to the refined unit-cell volumes of mirabilite and to the individual unit-cell parameters (with  $V_{P,T}$  replaced by  $a_{P,T}$ ,  $b_{P,T}$  *etc.*); the fitted parameters and the squared correlation coefficient ( $R^2$ ) are given in Table 2. The monoclinic angle  $\beta$  was fitted with a polynomial of the form  $\beta = \beta_0 + \beta_1 T + \beta_2 T^3 + \beta_3 P + \beta_4 TP$ , with coefficients  $\beta_0 = 108.01$  (1)°,  $\beta_1 = -1.36$  (6)  $\times 10^{-3}$ ° K<sup>-1</sup>,  $\beta_2 = 5.5$  (4)  $\times 10^{-9}$ ° K<sup>-3</sup>,  $\beta_3 = -3.7$  (1)  $\times 10^{-4}$ ° MPa<sup>-1</sup> and  $\beta_4 = 5.9$  (5)  $\times 10^{-7}$ ° K<sup>-1</sup> MPa<sup>-1</sup>.

A plot showing the observed pressure dependence of the relative volume,  $V/V_0$ , at 270 and 150 K, along with the BMEOS3  $P$ – $V$ – $T$  model evaluated at the same temperatures is shown in Fig. 2. A complete series of illustrations showing the fits to all quantities as a function of either  $P$  or  $T$  are provided in Supplementary Figs. S1–S3. Perspective views of these fitted surfaces as a function of  $P$  and  $T$ , with plots of the residuals, are shown in Fig. 3 and Supplementary Figs. S4–S8.

We had thought that the three-day interruption to the measurements during compression at 270 K (during which all of the pressure was lost on the specimen and had to be re-established) would lead to a discontinuity in the data. However, there is no evidence of any such discontinuity between the data acquired at 202 MPa, before the mains power cut, and that acquired at 247 MPa, after the power was restored. Nevertheless, there are some outlying points which we chose

to exclude from the EOS fit and these deserve comment. The first two points are in fact the first two measurements of the whole experiment, at 23 and 83 MPa, 270 K; the residuals in the BMEOS3 fit to  $P_{V,T}$  [circled in red in Figs. 3(b) and 3(c)] are, respectively, 5.7 and 7.3 times larger than the standard deviation of the fit ( $1\sigma = 1.89$  MPa). What is interesting is that the source of these misfits lies entirely with the  $c$  axis of the crystal. Supplementary Figs. S6(b) and S6(c) reveal that the same two data points lie  $7.5\sigma$  and  $7.7\sigma$ , respectively, away from the best fit through the rest of the  $c$ -axis data. It is only with the benefit of a broad data set collected as a function of  $P$  and  $T$  that these outliers become apparent. Our initial attempts to fit an isothermal EOS to the 270 K data, including the anomalous points, introduced a bias towards an implausibly small and ill-constrained  $K'$  for the volume ( $0.7 \pm 1.4$ ) and a negative  $K'$  for the  $c$  axis ( $-10 \pm 5$ ). Arguably, these first two data points could have been affected by initial permeation of helium into the crystal structure, although it is not clear why this would affect only the  $c$  axis. Furthermore, as we report below, the experimental bulk modulus is in excellent agreement with that predicted by density functional theory (DFT) calculations; if helium had penetrated the structure we would expect it to appear substantially more incompressible. We can only conclude, tentatively, that the first two outliers are the result of a similar dynamic process to that which leads to the difference in warming and cooling behaviour observed at room pressure (Brand *et al.*, 2009). The other two anomalous points are manifested solely in the values of the monoclinic angle  $\beta$  (Supplementary Figs. S7a and S7b). The points in question are at 543 MPa, 270 K, the last point on the compression curve, and 80 MPa, 150 K, the penultimate point collected on decompression: although the absolute values of the discrepancies in  $\beta$  are quite small ( $\sim 0.02$  and  $\sim 0.01$ °), the residuals associated with these points are, respectively, 4.6 and 7.0 times larger than the standard deviation of the fit. At

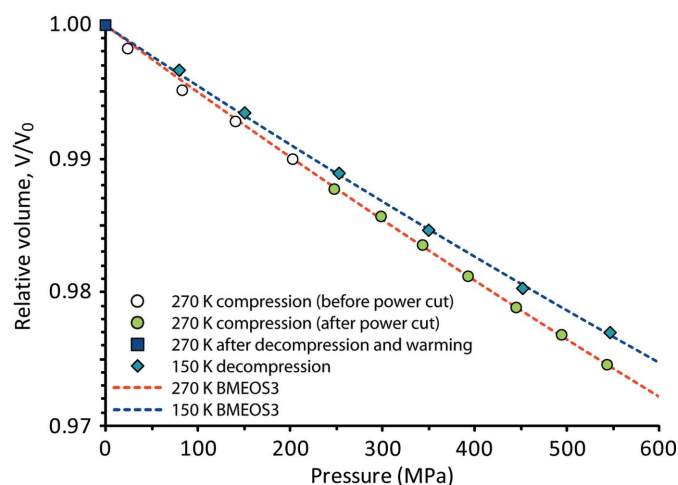


**Figure 2** Relative volume change in deuterated mirabilite on compression at 270 K and on decompression at 150 K. The dashed lines show isothermal slices through the  $P$ – $V$ – $T$  BMEOS3 fitted to the observations. Note the steeper slope at 270 K, indicating a greater compressibility than at 150 K. See text for a description of the events referred to in the figure legend that occurred during these measurements.

present we are not in a position to offer a firm explanation for these outliers, although it is worth observing that the first occurs immediately prior to the crystallization of ice IV, and the second immediately after the melting of ice IV, phenomena that may have introduced a small additional stress on the mirabilite component of the specimen.

Table 2 shows that there is a very satisfactory agreement between the volumetric values of  $K$  and  $K'$  obtained by experiment and by *ab initio* simulations, given that our observations are referenced to 270 K and the calculations were made in the athermal limit (Brand *et al.*, 2010). The pressure derivatives are, within errors, the same, and the bulk modulus – with due allowance for saturation as  $T$  falls to zero – may well be in the range 22–23 GPa at 0 K. Considering the low symmetry, the comparatively large unit cell (dominated by hydrogen), and the likely substantial effect of hydrogen bonding and orientational disorder on the properties of the material, this agreement between experiment and computer simulation is remarkable. The agreement, at least qualitatively, is also strikingly good for the elastic anisotropy; both the experiments and the calculations agree that the  $b$  axis is the stiffest, the  $c$  axis is the most compressible and the  $a$  axis falls between these two extremes. Note that Brand *et al.* (2010) did not report the  $a$ -axis EOS fit, only  $b$ ,  $c$  and  $a \sin \beta$ , but we have gone back to the original work and fitted these values for comparison. Table 2 also shows that  $K'$  for the  $a$  axis (as well as the direction  $a^* = a \sin \beta$ ) from the computational study is identical, within errors, to that found in this work, whilst the values of  $K'$  for the  $c$  axis differ considerably. The reader will

discern that, as a result of the restricted data set used in the present study,  $K'$  for the  $b$  axis has been fixed at the *ab initio* value in fitting the EOS to these data, for the following reasons. In a free fit of all parameters we found  $K' = 20 \pm 8$ . The large uncertainty in the parameter value is due in part to the lack of observational constraints (we could not use the HRPD data at all for this axis), and in part to the requirement to simultaneously fit  $\partial K'/\partial T$ . Since  $K'$  was so close to the computational prediction, we chose to fix the parameter at the *ab initio* value.

### 3.2. Elastic strain tensor

Since for a crystal of monoclinic or triclinic symmetry the axial elastic moduli alone do not necessarily yield an accurate picture of the relationship between compressional behaviour and the crystal structure, it is necessary to determine the shape and orientation of the elastic strain tensor. The elastic strain coefficients for a monoclinic crystal can be written as a symmetric second-rank tensor of the form

$$\begin{pmatrix} e_{11} & 0 & e_{13} \\ 0 & e_{22} & 0 \\ e_{31} & 0 & e_{33} \end{pmatrix}, \quad (6)$$

with  $e_{13} = e_{31}$ . The eigenvalues and eigenvectors of this matrix, obtained by matrix decomposition methods, are the magnitudes and orientations of the three principal axes of the elastic strain ellipsoid (*i.e.* directional compressibilities  $\beta_1$ ,  $\beta_2$  and  $\beta_3$ ) with respect to an orthogonal basis. We have applied the

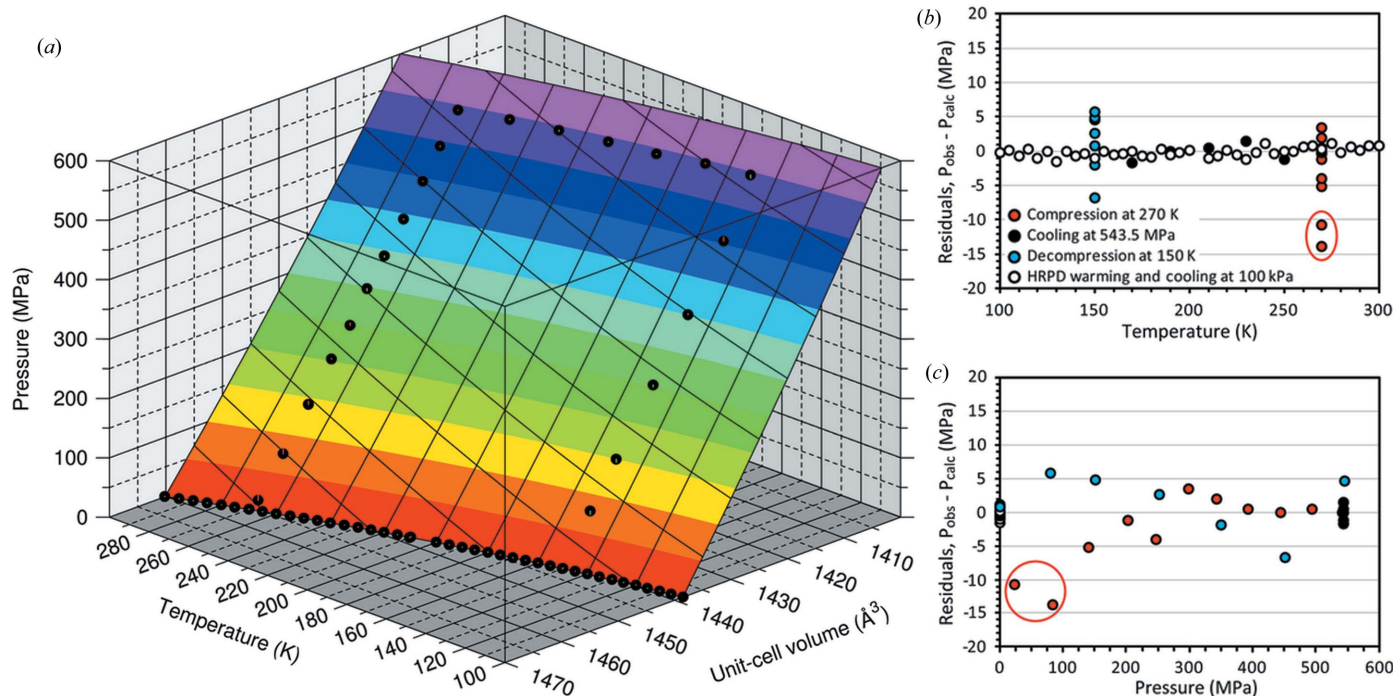


**Figure 3**

(a) Perspective view of the fitted  $P$ ,  $T$  dependence of the unit-cell volume of deuterated mirabilite; data points are shown as filled circles. Surface contours are in increments of 50 MPa. Parts (b) and (c) report the relative residuals as a function of pressure and temperature, respectively. Outlying points discussed in the main text are circled in red.

**Table 3**

$P$ ,  $T$  dependence, applicable within the range of our experimental measurements, of the incompressibility tensor's principal-axis magnitudes ( $\mathbf{K}_1$ ,  $\mathbf{K}_2$  and  $\mathbf{K}_3$ ), the bulk modulus ( $K_{\text{vol}}$ ), and the angle between  $\mathbf{K}_1$  and the  $X$  axis of the orthogonal reference basis (see Fig. 4), obtained from the BMEOS3  $P$ - $V$ - $T$  model.

Each term in column 1 has a pressure dependence of the form  $X_0 + X_1P + X_2P^2$  (where  $P$  is in GPa), and the temperature dependencies of  $X_0$ ,  $X_1$  and  $X_2$  are found using the expressions in columns 2–4. Note that  $T^* = T - 270$  K.

	$X_0$	$X_1P$	$X_2P^2$
$\mathbf{K}_1$ (GPa)	$58.8 - 0.089T^*$	$19.7 - 0.028T^*$	$3.9 - 0.005T^*$
$\mathbf{K}_2$ (GPa)	$81.6 - 0.085T^*$	$21.0 + 0.229T^*$	0
$\mathbf{K}_3$ (GPa)	$44.3 - 0.022T^*$	$20.8 + 0.006T^*$	$-2.8 - 0.002T^*$
$K_{\text{vol}}$ (GPa)	$19.3 - 0.018T^*$	$7.2 + 0.010T^*$	$-0.1 + 0.006T^*$
$\angle \mathbf{K}_1$ - $X$ ( $^\circ$ )	$13.1 - 0.015T^*$	$25.8 + 0.045T^*$	$-2.7 + 0.007T^*$

commonly used relationship between the orthogonal basis and the unit cell of a monoclinic crystal such that  $X \parallel a^*$ ,  $Y \parallel b$  and  $Z \parallel c$  (Boisen & Gibbs, 1990).

The  $P$ - $V$ - $T$  BMEOS3 model described in the previous section was used to compute a set of ‘smoothed’ unit-cell parameters as a function of pressure at four temperatures, 150, 190, 230 and 270 K. The method described by Hazen *et al.* (2000), implemented in a custom Microsoft *Excel* macro, was then employed to obtain the elastic strain coefficients, their principal axes and their orientations with respect to the orthogonal basis. The directional incompressibilities (*e.g.*  $\mathbf{K}_1 = \beta_1^{-1}$ ), the derived bulk modulus, and the angle between  $\mathbf{K}_1$  and the  $X$  axis of the orthogonal basis were fitted with simple polynomial functions as a function of  $P$  and  $T$  to yield the parameters reported in Table 3. Representation surfaces (Reynolds glyphs in the strict sense; see Hashash *et al.*, 2003) of the elastic strain at 270 K, 0.1 MPa and at 270 K, 550 MPa are shown in Figs. 4(a) and 4(b), with the disposition of the orthogonal axes, the unit-cell axes and the strain tensor's principal axes indicated by arrows. Note that there is a symmetry requirement that two principal axes must lie in the plane of the figure and the third must be perpendicular to it and that the distance from the origin to the edge of the representation surface indicates the compressibility in any given direction. At 270 K, 0.1 MPa, the most compressible direction ( $\beta_3$ ) is more closely aligned with the  $c$  axis. What is not evident from this illustration is that the least compressible direction ( $\beta_2$ ) is aligned with the  $b$  axis (out of the plane of the drawing), whereas the direction of intermediate compressibility ( $\beta_1$ ) is evidently more closely aligned to  $a^*$ , being inclined  $\sim 13^\circ$  from this direction, towards the  $c$  axis. The change upon increasing the pressure to 550 MPa, apart from a slight stiffening of the three principal axes, is a clockwise rotation of the strain tensor about the twofold axis of the crystal at a rate of  $\sim 26^\circ \text{ GPa}^{-1}$ .

For comparison of the elastic strain under compression with that generated by a change in temperature, we have included in Fig. 4(c) the thermal expansion representation surface evaluated at 270 K, 0.1 MPa using data from Brand *et al.* (2009). As one would expect, the direction of greatest thermal expansion corresponds closely to the direction of greatest compressibility, and that of least thermal expansion (perpen-

dicular to the diagram) with the least compressible direction in the crystal. The orientations of the representation surfaces are (crudely) similar, although it is worth noting that the thermal expansion tensor rotates clockwise at a high rate as the temperature nears the melting point (307.6 K for the deuterated crystal). Fig. 4(d) provides an illustration of mirabilite's crystal structure (after Levy & Lisensky, 1978), viewed along the  $b$  axis (with hydrogen atoms and all interstitial water molecules omitted for clarity). The structure consists of ribbons of edge-sharing  $\text{Na}(\text{H}_2\text{O})_6$  octahedra running parallel to the  $c$  axis, cross-linked by hydrogen bonds; sulfate tetrahedra lie between the ribbons of octahedra in the  $bc$  plane. It is apparent that the crystal compresses most readily along the axis of the edge-sharing ribbons. The structural information obtained from the *ab initio* simulations indicates that this is due to compression of the  $\text{Na}(\text{H}_2\text{O})_6$  octahedra rather than bending at the hinges between adjacent polyhedra; each of the two symmetry-inequivalent  $\text{Na}(\text{H}_2\text{O})_6$  units have polyhedral bulk moduli smaller than the bulk modulus of the crystal itself (19 and 14 GPa *versus* 22 GPa). With the present powder data set, we cannot distinguish between compression *versus* folding of the octahedral chains as an explanation for the compression along the  $c$  axis, and a high-pressure single-crystal study is required. The presence of very stiff tetrahedral  $\text{SO}_4^{2-}$  units (polyhedral bulk modulus  $\sim 170$  GPa; Brand *et al.*, 2010)

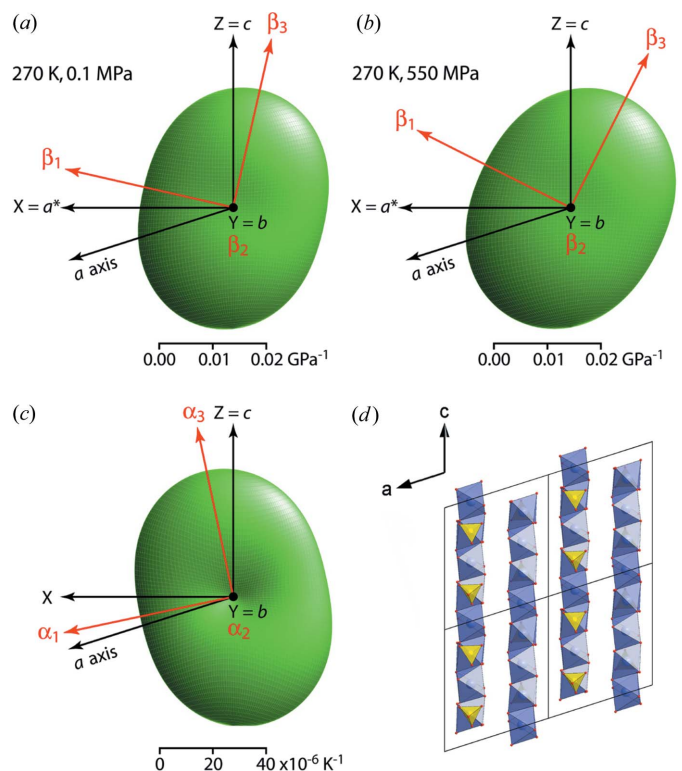


**Figure 4** Representation surfaces (Reynolds glyphs) of the compressibility at (a) 270 K, 0.1 MPa and (b) 270 K, 550 MPa; and (c) the thermal expansion at 270 K, 0.1 MPa. Black arrows indicate the orthogonal basis and the crystallographic axes, whilst grey (red in the electronic version) arrows denote the principal axes of the tensors. (d) The crystal structure of mirabilite viewed along the  $b$  axis, with H atoms and interstitial water molecules omitted.

between the ribbons apparently buttresses the structure parallel to the *b* axis, leading to the low compressibility in this direction.

### 3.3. Derivation of other thermodynamic quantities, $\gamma$ and $\delta^T$

With the aid of published data on the isobaric specific heat capacity of the protonated analogue of mirabilite (Brodale & Giauque, 1958) we are able to derive other useful material properties, such as the adiabatic bulk modulus ( $K^S$ ) and the Grüneisen parameter ( $\gamma$ ). The adiabatic bulk modulus is obtained from the isothermal bulk modulus ( $K^T$ ) as follows:

$$K^S = \frac{C_P K^T}{C_P - \alpha_V^2 V T K^T}, \quad (7)$$

where  $V$  is the molar volume ( $\text{m}^3 \text{mol}^{-1}$ ),  $\alpha_V$  is the volume thermal expansion coefficient ( $\text{K}^{-1}$ ) and  $C_P$  is the isobaric specific heat capacity ( $\text{J K}^{-1} \text{mol}^{-1}$ ). Having estimated  $K^S$  we calculate the thermodynamic Grüneisen parameter,  $\gamma$ , from

$$K^S = K^T (1 + \alpha_V \gamma T). \quad (8)$$

Finally, we use the fitted temperature dependence of the isothermal bulk modulus  $(\partial K^T / \partial T)_P$  to find the Anderson–Grüneisen parameter ( $\delta^T$ ):

$$\delta^T = \frac{1}{\alpha_V K^T} \left( \frac{\partial K^T}{\partial T} \right)_P. \quad (9)$$

This quantity is an important thermoelastic cross term that may be used to compute the thermal expansion at high pressure (*i.e.* as a function of molar volume):

$$(\alpha / \alpha_0) = (V / V_0)^{\delta^T}. \quad (10)$$

All of these derived quantities are given as a function of temperature in Table 4. For comparison with the  $P$ – $V$ – $T$  EOS, where  $K_{0,270}^T = 19.593 \text{ GPa}$  and  $(\partial K^T / \partial T)_P = -0.0175 \text{ GPa K}^{-1}$ , we find  $K_{0,270}^S = 19.995 \text{ GPa}$  and  $(\partial K^S / \partial T)_P = -0.0155 \text{ GPa K}^{-1}$ . Future measurement of the elastic constants of mirabilite will be required to verify these estimates. Furthermore, we find that  $\delta^T$  varies linearly with  $T$  above 250 K, but diverges from this linear dependence to larger values at lower temperatures, which we suspect is a result of the inaccuracy of assuming a linear  $(\partial K^T / \partial T)_P$ .

### 3.4. Thermal expansion and bulk modulus of ice IV

Ice IV, a nominally metastable hydrogen-bond-disordered ice polymorph with  $R\bar{3}c$  symmetry (Engelhardt & Whalley, 1972; Engelhardt & Kamb, 1978, 1981), was observed at ten  $P$ ,  $T$  points in the course of our study of mirabilite. This phase crystallized from what we assume to be a small amount of interstitial brine as the specimen was cooled from 270 to 250 K at 543 MPa, roughly in agreement – given the coarse temperature interval – with the known freezing point of the pure material (Mishima & Stanley, 1998). Ice IV persisted for a further 47 h as the temperature was reduced to 150 K (26 h) and the load reduced eventually to 80 MPa (21 h). Evans (1967) stated that ‘ice IV transforms to one of the stabler forms if stored for a few minutes at about  $-30^\circ\text{C}$ ’ (*i.e.* at

**Table 4**

Thermoelastic properties of deuterated mirabilite within the  $P$ ,  $T$  range of our experimental measurements, derived using a combination of literature data and our own measurements (see text for details).

$T$ (K)	$V^\dagger$ ( $\text{cm}^3 \text{mol}^{-1}$ )	$\alpha_V^\dagger$ ( $\times 10^{-6} \text{K}^{-1}$ )	$K_0^T$ (GPa)	$K_0^S$ (GPa)	$\gamma$	$\delta$	$C_P^\ddagger$ ( $\text{J mol}^{-1} \text{K}^{-1}$ )
280	219.378	98.68	19.42	19.84	0.79	9.13	544.94
260	218.971	92.77	19.77	20.15	0.80	9.54	513.07
240	218.584	86.87	20.12	20.46	0.81	10.01	480.89
220	218.209	80.96	20.47	20.77	0.82	10.56	448.39
200	217.870	75.05	20.82	21.08	0.83	11.19	415.58
180	217.549	69.14	21.17	21.39	0.84	11.95	382.46
160	217.266	63.24	21.52	21.70	0.85	12.85	349.03
140	217.004	57.33	21.87	22.02	0.87	13.95	315.28

$^\dagger$  Brand *et al.* (2009).  $^\ddagger$  Brodale & Giauque (1958).

$\sim 243 \text{ K}$ ; our italics). It is possible that in concentrated  $\text{Na}_2\text{SO}_4$  brine, the relative thermodynamic stabilities of ices IV and V are reversed, or else ice IV is stabilized by occlusion of the helium-pressure medium (*cf.* Londono *et al.*, 1992); it would, therefore, be most interesting to study the crystallization of high-pressure ice from  $\text{Na}_2\text{SO}_4$  solutions as a function of concentration and with other pressure media.

When the pressure was reduced from 150 to 80 MPa at 150 K, the Bragg peaks of ice IV disappeared; no reflections additional to those from mirabilite were observed in the 80 MPa data. Subsequently, when the pressure was reduced to 100 kPa, Bragg reflections from ice Ic appeared. This observation is consistent with the well established phenomenon of decompression-induced melting, observed in the case of both ice IV (at 105 MPa) and ice V (at 75 MPa); this has been attributed to the presence of a critical point in supercooled water, below which it is tentatively hypothesized that there is a phase transition between low-density and high-density liquid (Mishima & Stanley, 1998; Mishima, 2000; Dougherty, 2004). However, this steep  $(\partial T / \partial P \simeq \infty)$  melting line should ‘turn over’ below 170 K (*e.g.* Mishima, 2011), allowing ice IV to be recovered to atmospheric pressure at 150 K.

We were able to refine the unit-cell dimensions of ice IV to a precision of approximately 1 part in 30 000–40 000, and these results are given in Supplementary Table S2. Note that, because of the way that *GSAS* handles space-group operators, we have used the triply primitive hexagonal setting of the rhombohedral unit cell, although we have included the calculated values of  $a_R$  and  $\alpha$  for the rhombohedral cell for completeness. We have fitted a simple polynomial of the form  $V(T) = V_0 + a_1 T^2$  to the data collected on cooling, having found that inclusion of a term  $a_0 T$  led to a relative uncertainty in  $a_0 > 100\%$ . This fit yielded  $V_0 = 1076.6 (3) \text{ \AA}^3$  and  $a_1 = 4.79 (8) \times 10^{-4} \text{ \AA}^3 \text{K}^{-2}$ . Graphical representations of this fit and similar polynomial fits to the  $a_H$  and  $c_H$  axes are shown in Supplementary Fig. S9. The volume thermal expansion coefficient for ice IV at 543 MPa, which has not been reported previously at any pressure, is found by differentiation of the fitted  $V(T)$  curve to vary linearly from  $132 (2) \times 10^{-6} \text{ K}^{-1}$  at 150 K to  $217 (3) \times 10^{-6} \text{ K}^{-1}$  at 250 K. These values are similar to volumetric expansion coefficients reported for other stable and metastable ice phases that occur under the same  $P$ ,  $T$

conditions; Lobban (1998) reported  $\alpha_V = 240 (5) \times 10^{-6} \text{ K}^{-1}$  (500 MPa, 245.5 K) for ice V and  $\alpha_V = 270 (5) \times 10^{-6} \text{ K}^{-1}$  (500 MPa, 257.5 K) for ice XII.

We fitted an isothermal MILEOS to the decompression data for ice IV; least-squares minimization against all parameters led to  $K' = 12 (13)$ , the result primarily of having no constraint on the volume below 150 MPa. This parameter was fixed at  $K' \equiv 5$ , a reasonable value based on high-pressure studies of other icy polymorphs (e.g. Fortes *et al.*, 2005, 2012), from which we then find  $V_{0,150} = 1120.9 (6) \text{ \AA}^3$  and  $K_{0,150} = 16.6 (5) \text{ GPa}$  with a relatively small reduction in the fit quality ( $R^2$  drops from 0.99848 to 0.99816). This bulk modulus falls between the estimated zero-pressure bulk moduli of ice II and ice VI at 150 K, which are 13.2 and 17.2 GPa, respectively (Fortes *et al.*, 2005, 2009, 2012).

Our data also reveal that ice IV is highly isotropic in its elastic behaviour; the  $c/a$  ratio does not change significantly during cooling and changes by only 0.5% during decompression. This is almost identical in magnitude (but opposite in sign) to the relative change with pressure in the  $c/a$  ratio of ice II. The axial ratio for ice IV varies linearly as  $c/a = 1.9527 (5) + 1.76 (14) \times 10^{-5} P$  (at 150 K), yielding a decrease of 0.49% on decompression from 550 to 0.1 MPa: for ice II the axial ratio varies as  $c/a = 0.48304 (8) - 5.02 (23) \times 10^{-5} P$  (at 225 K;

Fortes *et al.*, 2005), yielding an increase of 0.57% on decompression over the same range.

Owing to the extent of the ice IV peak overlap with the predominant phase in our specimens, we could not extract any structural information on this phase, and a future detailed study of the structure of ice IV as a function of  $P$  and  $T$  is warranted.

#### 4. Discussion

The occurrence of soluble salts such as  $\text{Na}_2\text{SO}_4$  and  $\text{MgSO}_4$  in chondritic meteorites led to the hypothesis that aqueous alteration of chondritic rocks during the accretion and differentiation of some asteroids and icy planetary bodies would generate an abundance of brine; as these bodies cooled, the brines would crystallize a mixture of ices and salt hydrates, including mirabilite, epsomite ( $\text{MgSO}_4 \cdot 7\text{H}_2\text{O}$ ) and meridianiite ( $\text{MgSO}_4 \cdot 11\text{H}_2\text{O}$ ) as major ‘rock forming’ minerals (Kargel, 1991). The arguments for and against the presence of these salt hydrates has swung both ways over the past 20 years. Particularly for Jupiter’s icy satellite Europa, geochemical modelling favours a highly reduced subsurface ocean with negligible dissolved sulfate (Zolotov, 2012), although this may be ameliorated by downward mixing of radiolytically produced oxidants from the surface (Pasek & Greenberg, 2012). Nevertheless, there is observational evidence to support the original hypothesis; distorted  $\text{H}_2\text{O}$  absorption bands in the near infrared spectra of the Galilean satellites of Jupiter are best matched by the laboratory spectra of hydrated  $\text{Na}_2\text{SO}_4$ ,  $\text{MgSO}_4$  and  $\text{H}_2\text{SO}_4$  (e.g. Dalton, 2007; Dalton *et al.*, 2012; Orlando *et al.*, 2005; Shirley *et al.*, 2010). A number of theoretical models have demonstrated the importance of brines and salt hydrates, if they are present, in determining the structure, evolution and astrobiological potential of Jupiter’s icy moons (Kargel *et al.*, 2000; Prieto-Ballesteros & Kargel, 2005; Travis *et al.*, 2012). In particular, volume changes on melting or freezing of subsurface oceans in icy planetary bodies have been implicated in the formation of major global tectonic features on their surfaces (e.g. Consolmagno, 1985; Mitri *et al.*, 2010), including fracturing and rifting on Ganymede due to extensional stresses (global expansion) or thrusting and folding to form mountains on Titan due to compressional stress (global contraction).

From the perspective of this work, our  $P$ - $V$ - $T$  EOS can be used to calculate the density of the solid hydrate along each of the various high-pressure transition curves (Fig. 5), and this may be applied, in conjunction with an equivalent EOS for the co-existing aqueous phase (and any other relevant solid phase) to calculate the volume change on melting or freezing. An equation of state for aqueous  $\text{Na}_2\text{SO}_4$  exists, comprising no fewer than 41 parameters distributed across several publications (Chen *et al.*, 1977, 1980; Chen & Millero, 1981; Millero *et al.*, 1987), which is applicable over the ranges  $273 < T < 328 \text{ K}$ ,  $0.1 < P < 100 \text{ MPa}$  and  $0 < X < 1.5 \text{ mol kg}^{-1}$  (i.e. 0–17.56 wt%  $\text{Na}_2\text{SO}_4$ ). The majority of the high-pressure work on this aqueous system has been done at concentrations below 0.5  $M$  (6.63 wt%  $\text{Na}_2\text{SO}_4$ ), with the goal of determining the density

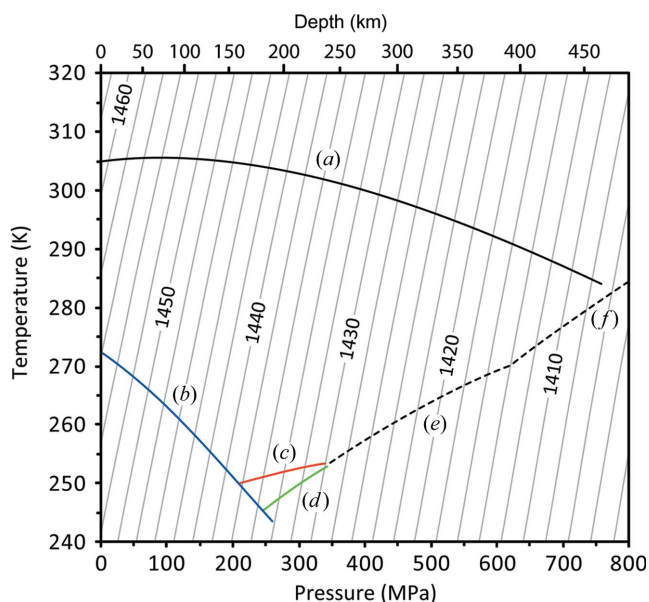


**Figure 5** Phase diagram illustrating the high-pressure transition curves for the system  $\text{Na}_2\text{SO}_4$ - $\text{H}_2\text{O}$ . The black line marked (a) is the melting line of mirabilite, which is incongruent up to 500 MPa and congruent at higher pressures. Refer to Supplementary Fig. S10 for the data used to obtain this melting curve. Lines (b), (c) and (d) are eutectics with ice reported by Dougherty *et al.* (2006, 2011, 2012), the first corresponding to coexistence with ice Ih, the second with ice III and the latter probably (although the authors are not certain) with ice V. The dashed line indicates the likely extensions of the eutectics between mirabilite and ice V (e) and ice VI (f), estimated from the pure ice melting curves (Bridgman, 1912). Grey diagonal lines show contours of constant unit-cell volume in deuterated mirabilite as determined from our  $P$ - $V$ - $T$  BMEOS3 fit (units  $\text{\AA}^3$ ). The scale along the top of the figure indicates the approximate depth in a fully differentiated icy satellite the size of Ganymede or Titan. For comparison, 800 MPa corresponds to a depth of  $\sim 25 \text{ km}$  in the Earth’s crust.

**Table 5**  
Molar volume of deuterated mirabilite along the transition lines indicated in Fig. 5.

Parameters are coefficients obtained by fitting an equation of the form  $V = a_0 + a_1P + a_2P^2 + a_3P^3$  to densities computed from the MILEOS  $P$ - $V$ - $T$ , the relative errors on the molar volume being obtained by propagation of the MILEOS parameter uncertainties.

	Transition lines marked in Fig. 5			
	Line (a)	Line (b)	Line (c)	Line (d)
$P$ range (MPa)	0–800	0–250	200–350	250–350
$a_0$ ( $\text{cm}^3 \text{mol}^{-1}$ )	219.9463	219.2230	218.5677	218.0729
$a_1$	$-1.13915 \times 10^{-2}$	$-1.27607 \times 10^{-2}$	$-9.64581 \times 10^{-3}$	$-7.51936 \times 10^{-3}$
$a_2$	$5.85128 \times 10^{-7}$	$-1.69800 \times 10^{-6}$	$-4.97010 \times 10^{-9}$	$-1.99212 \times 10^{-5}$
$a_3$	$4.65627 \times 10^{-10}$	$7.59905 \times 10^{-9}$	$2.59905 \times 10^{-10}$	0
Relative error	$4 \times 10^{-5}$ increasing to $5 \times 10^{-5}$ (500 Mpa) increasing to $1.4 \times 10^{-4}$ (800 Mpa)	$2 \times 10^{-5}$ increasing to $3 \times 10^{-5}$	$3 \times 10^{-5}$	$3 \times 10^{-5}$

of natural lake and sea waters. Schmidt (2009) reports densities of 1.54 M aqueous  $\text{Na}_2\text{SO}_4$  up to 1.1 GPa, but all except one point (the room  $P$ ,  $T$  reference point) are in the temperature range 373–873 K. However, we find that the 41-parameter EOS does reproduce the 298 K densities of 0.148 and 0.5 M solutions given by Abramson *et al.* (2001) up to 600 MPa within 0.5%. As a matter of interest, we tested the more recent room-pressure  $T$ ,  $X$  parameterization of the density (Clegg & Wexler, 2011), but found a negligible difference; the sum of squared residuals from the 298 K data of Abramson *et al.* (2001) dropped from  $1.42 \times 10^{-4}$  to  $1.39 \times 10^{-4}$ . In the absence of an alternative, we used the original 41-parameter  $P$ ,  $T$ ,  $X$  EOS to determine the liquid density along the mirabilite melting line (*i.e.* along the peritectic where melting is incongruent and on the melting line itself at higher pressure), with due consideration for the fact that both the concentrations (3.50–5.55 M) and the pressures (0–800 MPa) are far outside the stated range of applicability.

The molar volume of thenardite on the mirabilite melting line has been determined using the molar volume at room temperature (Rasmussen *et al.*, 1996) and the recently published elastic constant data of Arbeck *et al.* (2012). In fact our final result is comparatively insensitive to the properties of thenardite, since it represents only a small volume fraction of the mirabilite incongruent melt and this diminishes with pressure up to 500 MPa. Combined with the molar volume of mirabilite along the melting curve derived from this work (see Table 5), we compute the volume change of melting,  $\Delta V_m$ , for comparison with the values reported by Tammann (1903a,b) (Fig. 6). The volume change is positive below 82 MPa, but becomes negative at higher pressure, as expected from the change in slope of the melting curve; the slope shallows as the transition to congruent melting is reached, and then steepens at higher pressure. Although the observed  $\Delta V_m$  only extends to 275 MPa, it is clear that the slope of our calculated curve agrees with the data of Tammann (1903a,b), with an approximately constant offset. There are only two possible explanations for this offset: the first is that there is a difference in molar volume between the protonated and deuterated

analogues of mirabilite; the second is that there is a small systematic inaccuracy in the molar volumes obtained from the two neutron powder diffractometers, despite both being calibrated against NIST silicon standards prior to each set of measurements.

In order to test these hypotheses, we made X-ray powder diffraction measurements on samples of  $\text{Na}_2\text{SO}_4 \cdot 10\text{H}_2\text{O}$  and  $\text{Na}_2\text{SO}_4 \cdot 10\text{D}_2\text{O}$  (both prepared as described in §2) mixed with a  $\text{CaF}_2$  standard. Each measurement was made at  $248 \pm 1$  K on a PANalytical X’Pert Pro multi-purpose powder diffractometer (using Gemonochromated  $\text{Co K}\alpha_1$  radiation,  $\lambda = 1.788996 \text{ \AA}$ , and an X’Celerator multi-strip detector) equipped with a thermoelectrically cooled cold stage (Wood *et al.*, 2012). Refinement of the unit-cell parameters revealed an

extremely small difference in molar volume,  $\Delta V/V = 0.06$  (2)%, with the protonated species having the larger molar volume. Compare this with the difference of 0.33% between deuterated and protonated ice Ih at 265 K (Röttger *et al.*, 1994) and 0.56% between deuterated and protonated water at 273 K (Bridgman, 1935). The very small value we observe in mirabilite is not surprising, since the ‘free’ interstitial water is a relatively insubstantial part of the overall crystal structure. Whilst this reassures us that we can use D-mirabilite as a proxy for H-mirabilite, it also means that the offset in Fig. 6 is largely due to a systematic inaccuracy of around 0.3% in the absolute molar volumes.

We can achieve good agreement between the calculated and observed  $\Delta V_m$  and near perfect agreement with the measured enthalpy of the room-pressure transition mirabilite  $\rightarrow$

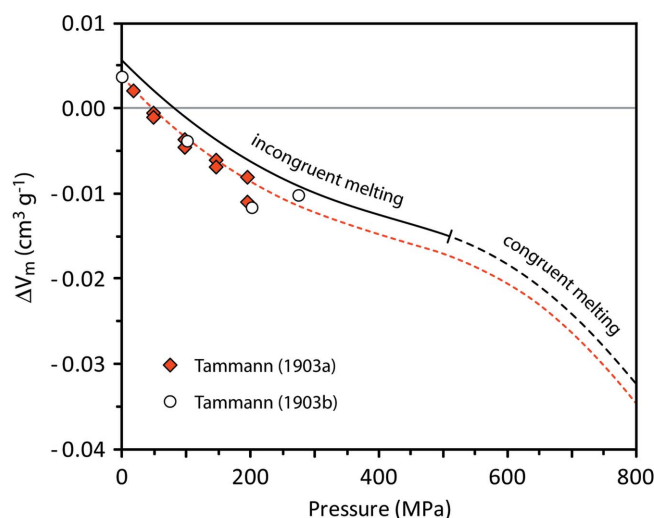


**Figure 6**  
The volume of melting,  $\Delta V_m$ , as a function of pressure calculated from our  $P$ - $V$ - $T$  EOS and the 41-parameter liquid EOS described in the text, compared with the only known measurements of this quantity by Tammann (1903a,b). The lower dashed line (red in the electronic version) indicates the calculated  $\Delta V_m$  when the molar volume of the solid hydrate is adjusted upward by 0.347%, as described in the text.

thenardite + brine,  $\Delta H_m = 78.97 \text{ kJ mol}^{-1}$  (Brodale & Giauque, 1958), by increasing the molar volume of mirabilite along the melting curve by +0.347%. Note that this is equivalent to approximately half the shift applied when we ‘corrected’ the OSIRIS refinements to match the HRPD refinements: in other words, the absolute molar volumes are almost exactly midway between those obtained from the two silicon-calibrated powder diffractometers. This illustrates the importance of making future measurements with an internal standard when a very high level of accuracy is required, as in this case. The shift in the calculated  $\Delta V_m$  is marked in Fig. 6 by the lower dashed line. We consider this to represent the most accurate prediction of  $\Delta V_m$  over the indicated pressure range. Using the Clausius–Clapeyron relation to compute  $\Delta H_m = (dP/dT)T\Delta V_m$  (where  $dP/dT$  is the slope of the pressure–melting curve, depicted along with the raw literature data in Supplementary Fig. S10), we find that the transition enthalpy halves, falling from  $79 \text{ kJ mol}^{-1}$  at room pressure to  $38 \text{ kJ mol}^{-1}$  at 500 MPa, where the melting becomes congruent. Above this pressure, the enthalpy of (congruent) melting rises once again, reaching  $45 \text{ kJ mol}^{-1}$  at 800 MPa. The limitations of the liquid equation of state, as it stands, preclude any further meaningful analysis.

Table 5 also provides a set of simple polynomial parameterizations of the molar volume of mirabilite along the experimentally determined eutectics. We cannot predict the volume change along these transition lines since there are presently no data on the compositional shift of these eutectics with pressure. Note that the values given by these polynomials do not include the *ad hoc* shift of 0.347% we applied to obtain agreement with the observed  $\Delta V_m$ . One or more measurements of the volume change on the eutectic would allow us to determine the robustness of this correction.

## 5. Conclusions

Using neutron powder diffraction methods, we have carried out the first experimental study to determine the elastic properties of sodium sulfate decadehydrate as a function of pressure and temperature. Importantly, we have shown that the difference in molar volume between H- and D-mirabilite is extremely small, so these findings are applicable to the ‘normal’ naturally occurring material. The  $P$  and  $T$  dependences of the unit-cell dimensions have been parameterized in terms of a third-order Birch–Murnaghan equation of state, and the parameters so obtained compare very favourably with those predicted by our earlier computational study using density functional theory, although the latter was formally done in the athermal limit. Furthermore, we have characterized the highly anisotropic strains resulting from the application of hydrostatic stress. Whilst we have been able to draw some general conclusions as to the causes of this anisotropy, high-pressure single-crystal measurements are justified in order to confirm our hypotheses. In particular, we have been unable to explain the softening of the  $b$  axis at low temperature and presently cannot rule out the possibility that it occurs as a result of some dynamical process related to orientational

disorder. Our thermal equation of state has allowed us to provide easily evaluated polynomial expressions for the variation in the molar volume both along the high-pressure melting curve and along the high-pressure eutectics with water ice. In combination with the available equation of state for aqueous  $\text{Na}_2\text{SO}_4$  (albeit extrapolated far beyond its limits of concentration and pressure), we have predicted the volume and entropy of melting of mirabilite as a function of pressure, which are important quantities in modelling the behaviour of a brine ocean inside an icy body. Both the change in sign of the volume change and the very substantial drop in the enthalpy of fusion ( $79 \text{ kJ mol}^{-1}$  at 100 kPa to  $38 \text{ kJ mol}^{-1}$  at 500 MPa) over the range of depths where such oceans are likely to exist in large icy satellites ( $\sim 50$ – $350 \text{ km}$ ) indicate the importance of our work for accurate planetary modelling. Clearly, assuming a constant enthalpy of fusion as a function of pressure would have a significant effect on the outcome of thermal evolutionary models.

There are, nonetheless, areas in which improvements are required. The equation of state for aqueous  $\text{Na}_2\text{SO}_4$  is inadequate for computing the properties of very concentrated solutions at the pressures likely to exist inside large icy satellites. A suitable equation of state should be applicable to concentrations of  $\sim 5 M$ , up to pressures of  $\sim 500 \text{ MPa}$  and down to temperatures of  $\sim 250 \text{ K}$ . Moreover, we require data on the compositional shift (if any) of the eutectics between mirabilite and various high-pressure ice phases, as well as measurements of the volume changes on those eutectics.

To our surprise, ice IV occurred as an accessory phase in our study. It is interesting to note that Heinz *et al.* (2007) also observed crystallization of ice IV, apparently as a stable phase, in aqueous solutions of ammonia, which transformed to ice VII on subsequent compression. This typically metastable ice polymorph may well be the stable phase of ice crystallizing from various concentrated aqueous solutions, in which case this hitherto poorly studied phase could be an important planetary mineral at depths of 300–350 km inside large icy satellites.

The authors thank the STFC ISIS facility for beam time and thank the ISIS Technical Support staff for their invaluable assistance. HEAB was funded by a postgraduate studentship from the Natural Environment Research Council, grant No. NER/S/A/2005/13554. ADF is supported by an advanced fellowship from the UK Science and Technology Facilities Council (STFC), grant No. PP/E006515/1.

## References

- Abramson, E. H., Brown, J. M., Slutsky, L. J. & Wiryana, S. (2001). *Int. J. Thermophys.* **22**, 405–414.
- Adams, L. H. (1938). *Am. J. Sci.* **35**, 1–18.
- Arbeck, D., Haussühl, E., Vinograd, V. L., Winkler, B., Paulsen, N., Haussühl, S., Milman, V. & Gale, J. D. (2012). *Z. Kristallogr.* **227**, 503–513.
- Birch, F. (1952). *J. Geophys. Res.* **57**, 227–286.
- Block, E. A. (1913). *Z. Phys. Chem. Stoechiom. Verwandtschaftsl.* **82**, 403–438.

- Bobade, S. M., Gopalan, P. & Kulkarni, A. R. (2009). *Ionics*, **15**, 353–355.
- Boisen, M. B. Jr & Gibbs, G. V. (1990). *Rev. Mineral.* **15**, 72–75.
- Brand, H. E. A., Fortes, A. D., Wood, I. G., Knight, K. S. & Vočadlo, L. (2009). *Phys. Chem. Miner.* **36**, 29–46.
- Brand, H. E. A., Fortes, A. D., Wood, I. G. & Vočadlo, L. (2010). *Phys. Chem. Miner.* **37**, 265–282.
- Bridgman, P. W. (1912). *Proc. Am. Acad. Arts Sci.* **47**, 441–558.
- Bridgman, P. W. (1935). *J. Chem. Phys.* **3**, 597–605.
- Brodale, G. & Giauque, W. F. (1958). *J. Am. Chem. Soc.* **80**, 2042–2044.
- Cadbury, W. E. (1945). *J. Am. Chem. Soc.* **67**, 262–268.
- Cadbury, W. E. (1955). *J. Phys. Chem.* **59**, 257–260.
- Cadbury, W. E., Meldrum, W. B. & Lucasse, W. W. (1941). *J. Am. Chem. Soc.* **63**, 2262–2267.
- Chen, C.-T. A., Chen, J. H. & Millero, F. J. (1980). *J. Chem. Eng. Data*, **25**, 307–310.
- Chen, C.-T. A., Fine, R. A. & Millero, F. J. (1977). *J. Chem. Phys.* **66**, 2142–2144.
- Chen, C.-T. A. & Millero, F. J. (1981). *J. Chem. Eng. Data*, **26**, 270–274.
- Clegg, S. L. & Wexler, A. S. (2011). *J. Phys. Chem. A*, **115**, 3393–3460.
- Consolmagno, G. J. (1985). *Icarus*, **64**, 401–413.
- Dalton, J. B. (2007). *Geophys. Res. Lett.* **34**, L21205.
- Dalton, J. B., Shirley, J. H. & Kamp, L. W. (2012). *J. Geophys. Res.* **117**, E03003.
- Derluyn, H., Saidov, T. A., Espinosa-Marzal, R. M., Pel, L. & Scherer, G. W. (2011). *J. Cryst. Growth*, **329**, 44–51.
- Dougherty, A. J., Avidon, A., Hogenboom, D. L. & Kargel, J. S. (2011). 42nd Lunar and Planetary Science Conference, 7–11 March 2011, The Woodlands, Texas, USA, abstract No. 1242.
- Dougherty, A. J., Avidon, A., Hogenboom, D. L. & Kargel, J. S. (2012). 43rd Lunar and Planetary Science Conference, 19–23 March 2012, The Woodlands, Texas, USA, abstract No. 2321.
- Dougherty, A. J., Hogenboom, D. L., Kargel, J. S. & Zheng, Y. F. (2006). 37th Lunar and Planetary Science Conference, 13–17 March 2006, League City, Texas, USA, abstract No. 1732.
- Dougherty, R. C. (2004). *Chem. Phys.* **298**, 307–315.
- Engelhardt, H. & Kamb, B. (1978). *J. Glaciol.* **21**, 51–53.
- Engelhardt, H. & Kamb, B. (1981). *J. Chem. Phys.* **75**, 5887–5899.
- Engelhardt, H. & Whalley, E. (1972). *J. Chem. Phys.* **56**, 2678–2684.
- Evans, L. F. (1967). *J. Appl. Phys.* **38**, 4930–4932.
- Fortes, A. D. & Choukroun, M. (2010). *Space Sci. Rev.* **153**, 185–218.
- Fortes, A. D., Wood, I. G., Alfredsson, M., Vočadlo, L. & Knight, K. S. (2005). *J. Appl. Cryst.* **38**, 612–618.
- Fortes, A. D., Wood, I. G., Tucker, M. G. & Marshall, W. G. (2012). *J. Appl. Cryst.* **45**, 523–534.
- Fortes, A. D., Wood, I. G., Vočadlo, L., Knight, K. S., Marshall, W. G., Tucker, M. G. & Fernandez-Alonso, F. (2009). *J. Appl. Cryst.* **42**, 846–866.
- Funk, R. (1900). *Ber. Deutsch. Chem. Ges.* **33**, 3696–3703.
- Geller, A. (1924). *Z. Kristallogr.* **60**, 415–472.
- Gibson, R. E. (1942). *Handbook of Physical Constants*, edited by F. Birch, J. F. Schairer & H. C. Spicer, Geological Society of America Special Papers, No. 36. New York: Geological Society of America.
- Hall, C. & Hamilton, A. (2008). *Icarus*, **198**, 277–279.
- Hamilton, A. & Hall, C. (2008). *J. Anal. Atom. Spectrom.* **23**, 840–844.
- Hamilton, A. & Menzies, R. I. (2010). *J. Raman Spectrosc.* **41**, 1014–1020.
- Hansen, T. C., Koza, M. M. & Kuhs, W. F. (2008). *J. Phys. Condens. Matter*, **20**, 285104.
- Hartley, H., Jones, B. M. & Hutchinson, G. A. (1908). *J. Chem. Soc. Trans.* **93**, 825–833.
- Hashash, Y. M. A., Yao, J. I.-C. & Wotring, D. C. (2003). *Int. J. Numer. Anal. Methods Geomech.* **27**, 604–626.
- Hazen, R. M., Downs, R. T. & Prewitt, C. T. (2000). *Rev. Mineral. Geochem.* **41**, 1–33.
- Heinz, D. L., Seagle, C. T., Campbell, A. J., Miller, N., Prakapenka, V. B. & Shen, G. (2007). AGU Fall Meeting, 10–14 December 2007, San Francisco, California, USA, abstract No. DI44A-07.
- Hogenboom, D. L., Kargel, J. S. & Pahalawatta, P. V. (1999). 30th Lunar and Planetary Science Conference, 15–19 March 1999, Houston, Texas, USA, abstract No. 1793.
- Kargel, J. S. (1991). *Icarus*, **94**, 369–390.
- Kargel, J. S., Kaye, J. Z., Head, J. W., Marion, G. M., Sassen, R., Crowley, J. K., Prieto-Ballesteros, O., Grant, S. A. & Hogenboom, D. L. (2000). *Icarus*, **148**, 226–265.
- Kryukov, P. A. & Manikhin, V. I. (1960). *Russ. Chem. Bull.* **9**, 2077–2078.
- Larsen, A. C. & Von Dreele, R. B. (2000). *General Structure Analysis System (GSAS)*. Report LAUR 86–748. Los Alamos National Laboratory, New Mexico, USA, <http://www.ncnr.nist.gov/xtal/software/gsas.html>.
- Levy, H. A. & Lisensky, G. C. (1978). *Acta Cryst.* **B34**, 3502–3510.
- Lobban, C. (1998). PhD thesis, University of London, UK.
- Londono, D., Finney, J. L. & Kuhs, W. F. (1992). *J. Chem. Phys.* **97**, 547–552.
- Malkin, T. L., Murray, B. J., Brukhno, A. V., Anwar, J. & Salzmann, C. G. (2012). *Proc. Natl Acad. Sci. USA*, **109**, 1041–1045.
- Meyer, J. & Aulich, W. (1928). *Z. Anorg. Allg. Chem.* **172**, 321–343.
- Millero, F. J., Vinokurova, F., Fernandez, M. & Hershey, J. P. (1987). *J. Solution Chem.* **16**, 269–284.
- Mishima, O. (2000). *Phys. Rev. Lett.* **85**, 334–336.
- Mishima, O. (2011). *J. Phys. Chem. B*, **115**, 14064–14067.
- Mishima, O. & Stanley, H. E. (1998). *Nature*, **392**, 164–168.
- Mitri, G., Bland, M. T., Showman, A. P., Radebaugh, J., Stiles, B., Lopes, R. M. C., Lunine, J. I. & Pappalardo, R. T. (2010). *J. Geophys. Res.* **115**, E10002.
- Murnaghan, F. D. (1944). *Proc. Natl Acad. Sci. USA*, **30**, 244–247.
- Orlando, T. M., McCord, T. B. & Grieves, G. A. (2005). *Icarus*, **177**, 528–533.
- Oswald, I. D., Hamilton, A., Hall, C., Marshall, W. G., Prior, T. J. & Pulham, C. R. (2008). *J. Am. Chem. Soc.* **130**, 17795–17800.
- Pasek, M. A. & Greenberg, R. (2012). *Astrobiology*, **12**, 151–159.
- Prieto-Ballesteros, O. & Kargel, J. S. (2005). *Icarus*, **173**, 212–221.
- Rasmussen, S. E., Jørgensen, J.-E. & Lundtoft, B. (1996). *J. Appl. Cryst.* **29**, 42–47.
- Richards, T. W. & Kelley, G. L. (1911). *J. Am. Chem. Soc.* **33**, 847–863.
- Richards, T. W. & Meldrum, W. B. (1921). *J. Am. Chem. Soc.* **43**, 1543–1545.
- Richards, T. W. & Wells, R. C. (1902). *Proc. Am. Acad. Arts Sci.* **38**, 431–440.
- Röttger, K., Endriss, A., Ihringer, J., Doyle, S. & Kuhs, W. F. (1994). *Acta Cryst.* **B50**, 644–648.
- Ruben, H. W., Templeton, D. H., Rosenstein, R. D. & Olovsson, I. (1961). *J. Am. Chem. Soc.* **83**, 820–824.
- Saidov, T. A., Espinosa-Marzal, R. M., Pel, L. & Scherer, G. W. (2012). *J. Cryst. Growth*, **338**, 166–169.
- Schmidt, C. (2009). *Geochim. Cosmochim. Acta*, **73**, 425–437.
- Shirley, J. H., Dalton, J. B., Prockter, L. M. & Kamp, L. W. (2010). *Icarus*, **210**, 358–384.
- Sood, R. R. & Stager, R. A. (1966). *Science*, **154**, 388–390.
- Tammann, G. (1903a). *Z. Phys. Chem.* **64**, 818–826.
- Tammann, G. (1903b). *Kristallisieren und Schmelzen: Ein Beiträge zur Lehre der Änderungen des Aggregatzustandes*. Leipzig: J. A. Barth.
- Tammann, G. (1929). *Z. Anorg. Allg. Chem.* **178**, 309–316.
- Tanaka, Y., Hada, S., Makita, T. & Moritoki, M. (1992). *Fluid Phase Equil.* **76**, 163–173.
- Taylor, H. S. (1934). *J. Am. Chem. Soc.* **56**, 2643.
- Telling, M. T. & Andersen, K. H. (2005). *Phys. Chem. Chem. Phys.* **7**, 1255–1261.
- Telling, M. T. F. & Anderson, K. H. (2008). *The OSIRIS User Guide*, 3rd ed. <http://www.isis.stfc.ac.uk/instruments/osiris/documents/osiris-user-guide6672.pdf>.
- Toby, B. H. (2001). *J. Appl. Cryst.* **34**, 210–213.

- Travis, B., Palguta, J. & Schubert, G. (2012). *Icarus*, **218**, 1006–1019.
- Wood, I. G., Brand, H. E. A., Fortes, A. D., Vočadlo, L. & Gutmann, M. (2010). ISIS Experimental Report RB 910178. Rutherford Appleton Laboratory, Didcot, Oxfordshire, UK.
- Wood, I. G., Hughes, N. J., Browning, F. & Fortes, A. D. (2012). *J. Appl. Cryst.* **45**, 608–610.
- Wood, I. G., Vočadlo, L., Dobson, D. P., Price, G. D., Fortes, A. D., Cooper, F. J., Neale, J. W., Walker, A. M., Marshall, W. G., Tucker, M. G., Francis, D. J., Stone, H. J. & McCammon, C. A. (2008). *J. Appl. Cryst.* **41**, 886–896.
- Zhilova, S. B., Karov, Z. G. & El'mesova, R. M. (2008). *Russ. J. Inorg. Chem.* **53**, 628–635.
- Zolotov, M. Yu. (2012). *Icarus*, **212**, 713–729.